Active Disturbance Rejection Control of Photovoltaic Three-Phase Grid Following Inverters Under Uncertainty and Grid Voltage Variations

Jitendra Kumar Singh ⓘ, *Member, IEEE*, Surya Prakash ⓘ, *Graduate Student Member, IEEE*, Khaled Al Jaafari ⓘ, *Senior Member, IEEE*, Omar Al Zaabi ⓘ, *Member, IEEE*, Khalifa Al Hosani ⓘ, *Senior Member, IEEE*, Ranjan Kumar Behera ⓘ, *Senior Member, IEEE*, and Utkal Ranjan Muduli ⓘ, *Senior Member, IEEE*

Abstract—A PV three-phase grid following inverter (GFI) with LCL filters can reduce current harmonics and deliver active power to the grid. Controlling such higher-order systems is challenging due to system uncertainties, grid voltage variations, and filter resonance. Active disturbance rejection control (ADRC) provides resilience to these uncertainties and a prompt response to disturbances. A linear extended state observer and a phase-locked loop observer are integrated into the ADRC structure to optimize tracking performance. The proposed controller uses a structured inner and outer closed-loop ADRC that takes into account process delays and extended state observer dynamics. The GFI can operate under variable grid voltage frequencies or even deviations in frequency caused by grid failure, and is able to meet these challenges as part of the design process and the synchronization approach. Both simulation and experimental results are given to validate the dual ADRC-based methods for an 8 kW laboratory prototype PV-GFI system.

Index Terms—Active disturbance rejection controller, grid following inverter, grid synchronization, grid voltage disturbance, photovoltaic system.

I. INTRODUCTION

ADVANCEMENTS in smart grid technology promote the integration of distributed generation systems, including renewable energy sources like photovoltaics and wind power.

Jitendra Kumar Singh, Surya Prakash, and Ranjan Kumar Behera are with the Department of Electrical Engineering, Indian Institute of Technology Patna, Bihta 801103, India (e-mail: jitendra1603@gmail.com; suryaprakashele@gmail.com; rkb@iitp.ac.in).

Khaled Al Jaafari, Omar Al Zaabi, Khalifa Al Hosani, and Utkal Ranjan Muduli are with the Department of Electrical Engineering and Computer Science, Khalifa University, Abu Dhabi 127788, UAE (e-mail: khaled.aljaafari@ku.ac.ae; omar.alzaabi@ku.ac.ae; khalifa.halhosani@ku.ac.ae; utkal.muduli@ku.ac.ae).

These energy sources connect to the grid at the point of common coupling using grid following inverter (GFI) and LCL-type input filters. While LCL filters improve grid power quality by reducing high-frequency switching components [1], they introduce control complexity and resonance issues. Ensuring high-quality grid-injected currents requires careful design of both the GFI and its associated controller to maintain reliable operation under various disturbance scenarios [2], [3].

A variety of approaches have been proposed to estimate and mitigate disturbance effects on physical GFI systems [4], [5], with active disturbance rejection control (ADRC) being a suitable solution. ADRC's high noise attenuation capability impacts controller dynamics during parameter uncertainties [4], and when based on an extended state observer (ESO), it can estimate uncertainties and external disturbances, enhancing GFI system dynamics [5]. ESO and third-order ADRC demonstrate strong robustness against internal and external disturbances. Control methodologies in [6] and [7] effectively address imbalanced grid voltage and filter parameters using a combination of disturbance observers and a current controller. A higher-order linear ESO (LESO), called generalized ESO (GESO), compensates for total disturbance with minimal tracking error, improving system dynamics without relying on an accurate system model [8]; however, stability margin decreases as ESO order increases [8].

To enhance GFI stability, voltage sensorless control coupled with a grid-side current controller offers optimal performance while reducing hardware complexities [9]. Despite these techniques achieving sensorless grid voltage operation, output currents remain highly sensitive to system parameter variations. Employing only grid-side current sensor installation, these systems utilize robust current management algorithms and disturbance observers (DOBs) to estimate grid voltage and state variables, successfully stabilizing LCL filtered GFIs under internal and external disturbances. However, none of the previously proposed robust control methods have considered grid frequency variation as a significant disturbance source during grid faults. Furthermore, a high disturbance rejection capability diminishes the observer's bandwidth, subsequently degrading system dynamics. The phase-locked-loop (PLL) dynamics, used for grid synchronization, impair system stability in weak grid

conditions [10], and PLL-less current control discussed in [11] is more suitable for ideal grid conditions while remaining sensitive to a wide range of grid impedance variations and parametric perturbations. The paper's objective is to investigate appropriate grid frequency and phase angle estimation under disturbance scenarios to increase GFI system stability. An ADRC-based controller effectively mitigates power fluctuations from maximum power point tracking (MPPT) and improves system dynamics under grid disturbances [12]. Three-phase single-stage PV integrated systems produce low-frequency ripple at the DC-link and variable instantaneous active power, resulting in distorted and unbalanced grid current. Maintaining a stable DC-link under internal and external disturbances is essential for reliable PV integrated GFIs [13]. PV-generated current often surpasses grid-injected current, causing energy accumulation in the DC-link capacitor. Feedback linearization with sliding mode control limits DC-link voltage under grid disturbances [13]. During grid voltage sag, a robust DC-link controller is needed for stable DC-link voltage under MPP deviation-induced disturbances. Conventional ADRC-applied PV-GFI systems suffer from parameter uncertainties and external disturbances due to PV intermittency. LESO-based ADRC, as discussed in [14], improves noise filtering capability but may compromise stability with large gain and increased controller order. An enhanced ESO featuring a simple proportional gain that reduces the controller's order can boost stability with less complexity [15].

Inverter-side current control using reduced-order model-based linear ADRC with capacitor current active damping is presented in [16], requiring extra current and voltage sensors for LCL filter resonance damping. The weighted average current strategy in [17] improves system robustness under weak grid conditions, but still necessitates additional sensors. An ESO-based ADRC in [18] aims to mitigate resonance phenomena by estimating output and lumped disturbances with online disturbance rejection. However, handling unexpected grid disturbances and PV intermittency remains a challenge. Considering the above objectives, the original contributions of the article can be summarized as follows.

- Both DC-side and AC-side modelling of the PV-GFI are analyzed in dq-domain by considering the system parameter uncertainties and unknown grid disturbances.
- A utilization of LESO and PLL based observer (PLLO) with the proposed outer ADRC is investigated to control the DC-link voltage, considering the uncertainties due to the photovoltaics and the grid voltage.
- A proposed inner ADRC employs reduced-order ESO (RESO) and PLLO to control grid current injection at PCC by estimating grid voltage disturbances. This controller enables the estimation of the grid voltage phase angle and frequency without external PLL, using the normalized value of internally generated grid disturbance.

Section II delves into the modeling of the PV-GFI system. The proposed inner and outer ADRCs, as well as stability analysis, are detailed in Section III. Section IV presents pertinent results and discussions, with conclusions provided in Section V.
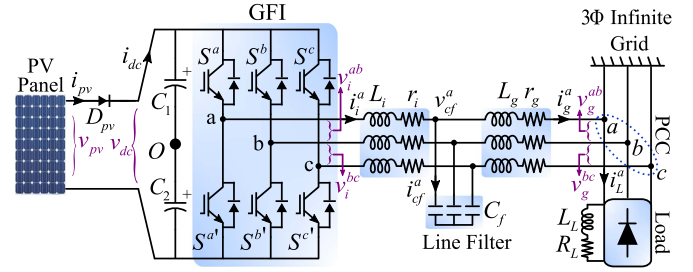

Fig. 1. Schematic of single-stage three-phase PV-GFI.

II. GFI MODELLING ASPECT

A. System Description

Fig. 1 illustrates a three-phase GFI configuration comprising the dc-link capacitor (C_{dc}), the VSI, and the LCL filter. The grid-side inductor (L_g) and the inverter-side inductor (L_i) include the parasitic resistances r_g and r_i, respectively, though their effects can be disregarded in worst-case scenarios. The capacitor of (C_f) the LCL filter plays a crucial role in harmonic attenuation, resonance frequency determination, damping, reactive power compensation, and voltage stability. v_{cf}^x and i_{cf}^x are the voltage across and current through the filter capacitor of LCL filter. The currents through these inductors are represented as i_g^x and i_i^x, while the potentials at the PCC and GFI terminals are denoted as v_g^x and v_i^x, respectively. The GFI terminal voltage depends on the DC-link voltage (v_{dc}) and the switching function (s_i^x) generated by the proposed controller: $v_i^x = s_i^x v_{dc}$. This switching function s_i^x governs the switching pulse for each GFI switch $S^a, S^{a'}, S^b, S^{b'}, S^c, S^{c'}$, as depicted in Fig. 1.

1) GFI AC-side Modeling: Let $\{a, b, c\}$, $\{\alpha, \beta\}$ and $\{d, q\}$ denote the superscripts corresponding to the three-phase, $\alpha\beta$-plane and dq-plane, respectively. The phase transformation from $abc \rightarrow \alpha\beta$ and $\alpha\beta \rightarrow dq$ can be represented as given in (1).

$$X^{\alpha\beta} = X^\alpha + jX^\beta = \sqrt{\frac{2}{3}} \sum_{\substack{k=1 \\ x\in\{a,b,c\}}}^{3} X^x e^{j\frac{2\pi}{3}(k-1)}$$

$$X^{dq} = X^d + jX^q = e^{-j\hat{\theta}_g} X^{\alpha\beta} \tag{1}$$

where X denotes the variables $\{v : \text{voltage}, i : \text{current}, s : \text{switching function}\}$. j is considered a complex operator, and the superscript $[]^{dq}$ corresponds to a complex variable $[]^d + j[]^q$. $x \in \{a, b, c\}$ represent the subscripts for the three phases, and $k \in \{1, 2, 3\}$ represents the subsequent phase number. The phase angle ($\hat{\theta}_g$) and the amplitude ($\hat{v}_{gm}$) of the PCC voltage (v_g^x) can be accurately estimated using the appropriate PLL mentioned in [19].

Now, the ac side dynamics of GFI with state variables i_i^x, i_g^x, v_{cf}^x and v_{dc} can be represented as (2).

$$\dot{i}_i^x = -\tau_i^{-1} i_i^x + L_i^{-1} \left(-v_{cf}^x + s_i^x v_{dc} \right)$$

$$\dot{i}_g^x = -\tau_g^{-1} i_g^x + L_g^{-1} \left(v_{cf}^x - v_g^x \right)$$

$$\dot{v}_{cf}^x = C_f^{-1} \left(i_i^x - i_g^x \right) \tag{2}$$

where τ_i $(= L_i/r_i)$ and τ_g $(= L_g/r_g)$ represent the time constants. As τ_i and τ_g are significantly higher with low parasitic resistance value r_g and r_i, respectively, the corresponding term in (2) can be neglected and the GFI model can be further modified as (3).

$$
\begin{aligned}
\dot{i}_i^x &= L_i^{-1}\left(-v_{cf}^x + s_i^x v_{dc}\right) \\
\dot{i}_g^x &= L_g^{-1}\left(v_{cf}^x - v_g^x\right) \\
\dot{v}_{cf}^x &= C_f^{-1}\left(i_i^x - i_g^x\right)
\end{aligned}
\tag{3}
$$

Eq. (3) represents the state-space representation of the GFI system in the abc-domain. In the dq-domain, the state-space model can be obtained as (4).

$$
\begin{aligned}
\dot{i}_i^{dq} &= -j\hat{\omega}_g i_i^{dq} + L_i^{-1}\left(-v_{cf}^{dq} + s_i^{dq} v_{dc}\right) \\
\dot{i}_g^{dq} &= -j\hat{\omega}_g i_g^{dq} + L_g^{-1}\left(v_{cf}^{dq} - v_g^{dq}\right) \\
\dot{v}_{cf}^{dq} &= -j\hat{\omega}_g v_{cf}^{dq} + C_f^{-1}\left(i_i^{dq} - i_g^{dq}\right)
\end{aligned}
\tag{4}
$$

where $\hat{\omega}_g$ is the estimated angular grid frequency. It is obvious that s_i^{dq} denotes the control input and i_g^{dq} is the output of the overall PV-GFI system. The effect due to the grid voltage is completely considered a disturbance in the further problem formulation. In further modeling, the LCL filter parameters are considered with uncertainties, i.e., $L_i = L_{i0} + \Delta L_i$, $L_g = L_{g0} + \Delta L_g$ and $C_f = C_{f0} + \Delta C_f$. Here, L_{i0}, L_{g0} and C_{f0} denote the nominal parameter values and Δ indicate the parameter uncertainties. Implementing these modifications in (4), the modeling of the GFI system can be further represented as (5).

$$
\begin{aligned}
\dot{i}_i^{dq} &= -j\hat{\omega}_g i_i^{dq} + L_{i0}^{-1}\left(-v_{cf}^{dq} + s_i^{dq} v_{dc}\right) + \psi_i^{dq} \\
\dot{i}_g^{dq} &= -j\hat{\omega}_g i_g^{dq} + L_{g0}^{-1}\left(v_{cf}^{dq} - v_g^{dq}\right) + \psi_g^{dq} \\
\dot{v}_{cf}^{dq} &= -j\hat{\omega}_g v_{cf}^{dq} + C_{f0}^{-1}\left(i_i^{dq} - i_g^{dq}\right) + \psi_{cf}^{dq}
\end{aligned}
\tag{5}
$$

where ψ_i^{dq}, ψ_g^{dq} and ψ_{cf}^{dq} denote the uncertainties due to variations in the GFI system parameters. Internal and external disturbances are treated as a single lumped disturbance in ADRC, which is then evaluated by an observer and eliminated in real time via the control input. The uncertain GFI model is first converted into an integral chain form, as given in (6)–(11).

$$
x_1^{dq} = i_g^{dq}
\tag{6}
$$

$$
\dot{x}_1^{dq} = x_2^{dq} = \dot{i}_g^{dq}
$$

$$
= -j\hat{\omega}_g i_g^{dq} + L_{g0}^{-1}\left(v_{cf}^{dq} - v_g^{dq}\right) + \psi_g^{dq}
$$

$$
= -j\hat{\omega}_g x_1^{dq} + L_{g0}^{-1}\left(v_{cf}^{dq} - v_g^{dq}\right) + \psi_g^{dq}
\tag{7}
$$

$$
\dot{x}_2^{dq} = x_3^{dq} = -j\hat{\omega}_g x_2^{dq} + L_{g0}^{-1}\left(\dot{v}_{cf}^{dq} - \dot{v}_g^{dq}\right) + \psi_1^{dq}
$$

$$
= -j\hat{\omega}_g x_2^{dq} + L_{g0}^{-1}C_{f0}^{-1}\left(i_i^{dq} - i_g^{dq}\right) + \psi_2^{dq}
\tag{8}
$$

$$
\dot{x}_3^{dq} = -j\hat{\omega}_g x_3^{dq} + L_{g0}^{-1}C_{f0}^{-1}\left(\dot{i}_i^{dq} - \dot{i}_g^{dq}\right) + \psi_3^{dq}
$$

$$
= \underbrace{-j\hat{\omega}_g x_3^{dq} - \omega_r^2 x_2^{dq}}_{\text{Known disturbance}} + b_0 s_i^{dq} + x_4^{dq}
\tag{9}
$$

$$
\dot{x}_4^{dq} = h^{dq}
\tag{10}
$$

$$
y_o^{dq} = x_1^{dq}
\tag{11}
$$

where ω_r $\left(= \sqrt{C_{f0}^{-1}(L_{g0}^{-1} + L_{i0}^{-1})}\right)$ and ω_a $\left(= \sqrt{L_{g0}^{-1}C_{f0}^{-1}}\right)$ are the resonant angular frequency and the antiresonant angular frequency. b_0 $(= L_{i0}^{-1}\omega_a^2 v_{dc})$ is considered the control gain of the control input s_i^{dq}. ψ_1^{dq} $(= -j\dot{\hat{\omega}}_g x_1^{dq} + \dot{\psi}_g^{dq})$, ψ_2^{dq} $(= \psi_1^{dq} + L_{g0}^{-1}(-j\hat{\omega}_g v_{cf}^{dq} + \psi_{cf}^{dq} - \dot{v}_g^{dq}))$, ψ_3^{dq} $(= -j\dot{\hat{\omega}}_g x_2^{dq} + \dot{\psi}_2^{dq})$ and ψ^{dq} $(= \psi_3^{dq} + \omega_a^2(-j\hat{\omega}_g i_i^{dq} - \psi_i^{dq} + \psi_g^{dq}))$ are the combined effect of all uncertainties and unknown disturbances. The disturbance ψ^{dq} cannot be measurable in real time and requires an implementation of ESO. As discussed in Section III-A, inner ADRC introduces ESO to estimate $\hat{\psi}^{dq}$ to nullify the impact of ψ^{dq}. As shown in (9)–(10), s_i^{dq} and y_o^{dq} can be the input and output of the ESO with the assumption that the extended state $x_4^{dq} = \psi^{dq}$ is differentiable and $h^{dq} = \dot{\psi}^{dq}$ is bounded. Now, the state-space model can be represented as (12) which can be used in further detail for the inner ADRC design in Section III-A.

$$
\dot{X}^{dq} = AX^{dq} + Bs_i^{dq} + Dh^{dq}; \quad Y^{dq} = CX^{dq}
\tag{12}
$$

where X^{dq} $(= [x_1^{dq}, x_2^{dq}, x_3^{dq}, x_4^{dq}]^T)$ and Y^{dq} are the internal state and output of the GFI system in dq-frame. A, B, C and D are the system matrix, the input matrix, the output matrix and the disturbance matrix, respectively, and can be defined as follows.

$$
A = \begin{bmatrix} 0 & 1 & 0 & 0 \\ 0 & 0 & 1 & 0 \\ 0 & -\omega_r^2 & -j\hat{\omega}_g & 1 \\ 0 & 0 & 0 & 0 \end{bmatrix} \quad B = \begin{bmatrix} 0 \\ 0 \\ b_0 \\ 0 \end{bmatrix} \quad C = \begin{bmatrix} 1 \\ 0 \\ 0 \\ 0 \end{bmatrix}^T \quad D = \begin{bmatrix} 0 \\ 0 \\ 0 \\ 1 \end{bmatrix}
$$

2) GFI DC-Side Modeling: The ac-side GFI current can be seen as (13) at the DC-link of the GFI.

$$
i_{dc} = \sum_{x \in \{a,b,c\}} s_i^x i_i^x
\tag{13}
$$

where i_{dc} is the current on the DC side of the GFI. The DC-side dynamics of the GFI can be represented as (14).

$$
\dot{v}_{dc} = C_{dc}^{-1}\left(-\sum_{x \in \{a,b,c\}} s_i^x i_i^x + i_{pv}\right)
\tag{14}
$$

In addition, the dq-transformation from (1) is applied to simplify (14) as (15).

$$
\dot{v}_{dc} = C_{dc}^{-1}\left(-\Re\left\{s_i^{dq}\bar{i}_i^{dq}\right\} + i_{pv}\right)
\tag{15}
$$

where $\Re$ and $\bar{\ }$ denote the notation of the real component and conjugate of a complex variable. The power rating of C_f in an LCL-type GFI system is supposed to be 5% of the rated power of GFI [20]. Under steady-state conditions, i_i^{dq} is approximately equal to i_g^{dq}. Taking into account the effect of grid current (i_g^{dq}) on
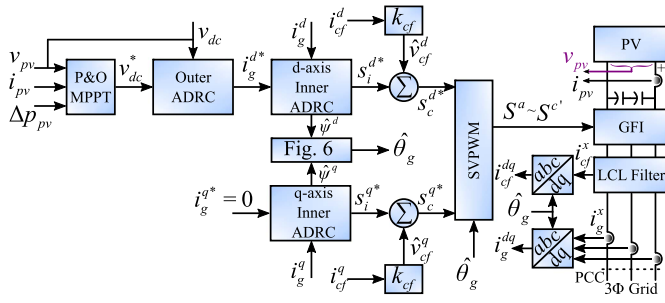
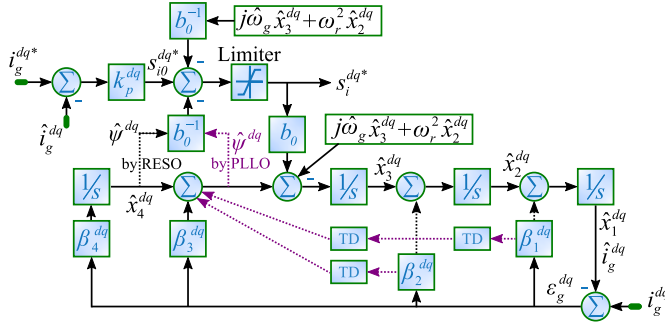Fig. 2.   Proposed control strategy for the PV-GFI system.

Fig. 3.   Inner ADRC schematic with both RESO (black dotted lines) and PLLO (pink dotted lines) implementation.

i_i^{dq} (i.e., $\chi_f i_g^{dq}$) during steady state, (15) can be further simplified as (16).

$$\dot{v}_{dc} = C_{dc}^{-1} \left(-\Re \left\{ \chi_f s_i^{dq} \bar{i}_g^{dq} \right\} + i_{pv} \right) \qquad (16)$$

where χ_f is considered the short circuit reverse current gain during the steady state period and can be derived as (17).

$$\chi_f = \left. \frac{1}{1 + L_f C_f s^2} \right|_{s=j\hat{\omega}_g} = \frac{1}{1 - L_f C_f \hat{\omega}_g^2} \qquad (17)$$

Now, (16) can be simplified to (18) to establish the relation for the development of the outer ADRC.

$$\begin{aligned} \dot{v}_{dc} &= C_{dc}^{-1} \left(-\chi_f \left(s_i^d i_g^d + s_i^q i_g^q \right) + i_{pv} \right) \\ &= b_i i_g^{d*} + \hat{\psi}_v^{dc} \end{aligned} \qquad (18)$$

where $b_i \ (= C_{dc}^{-1} \chi_f s_i^d)$ is the control gain of the control input i_g^{d*} and $\hat{\psi}_v^{dc} \ (= C_{dc}^{-1}(-\chi_f(s_i^d i_g^d + s_i^d i_g^{d*} + s_i^q i_g^q) + i_{pv}))$ represent unmodeled dynamics due to solar photovoltaics, filter parameter variations and grid uncertainty.

III. PROPOSED CONTROL METHODOLOGY

Instead of conventional proportional integral (PI)-based controllers, this paper uses one first-order ADRC and one reduced-order ADRC. The structural block diagram of the overall control structure along with these ADRCs are provided in Fig. 2 and is described with the following methodology.

Step 1: Measure v_{pv} (i.e. DC-link voltage v_{dc}), i_{pv} and incremental change in PV power (ΔP_{pv}) and apply the appropriate incremental conductance MPPT control mentioned in [21] to generate the reference DC link voltage (v_{dc}^*).

Step 2: Utilize First-order ADRC in the outer loop to control v_{dc} with respect to v_{dc}^* against sudden disturbances, either by photovoltaics or by grid voltage.

Step 3: Measure the grid current i_g^x, $x \in \{a, b, c\}$ and the current through the filter capacitor i_{cf}^x. Then, further apply the dq-transformation from (1) to get i_g^{dq} and i_{cf}^{dq}, where the grid phase angle $\hat{\theta}_g$ is generated from inner ADRC.

Step 4: To control the current dynamics, a reduced-order ADRC is employed in the inner loop, accounting for disturbances associated with system parameter variations and grid voltage uncertainties. The outer loop provides a current reference (i_g^{d*}) to the inner loop for precise grid current control of i_g^{dq}, with i_g^{q*} considered zero since no reactive power is supplied through this controller. The proposed controller's performance is supported by the following assumptions: 1) Nonlinearities in saturation and deformity in line filters are considered disturbances. 2) All disturbances and their higher derivatives must be uniformly bounded [22]. 3) The current i_g^d is regarded as 'zero' due to the faster inner current loop dynamics compared to the outer voltage loop; the PV-GFI system will malfunction if i_g^q exceeds a safety threshold of 1.2 pu. 4) Large variations in load demand can cause current constraint violations, as the current is directly affected by power demand changes; thus, it is assumed that the required load power p_L varies within a range related to i_g^q [23].

Step 5: Generate $\hat{v}_{cf}^{dq}$ by multiplying a constant gain k_{cf} by i_{cf}^{dq}. This implements an active damping concept to compensate for the loss component in the filter capacitor.

Step 6: Implement an SVPWM strategy to generate switching pulses ($S^a \cdots S^{c'}$) for the GFI system, where the input to SVPWM is the compensated switching function s_c^{dq*} ($s_i^{dq*} + \hat{v}_{cf}^{dq}$). The switching function s_i^{dq*} is generated from the inner ADRC as explained later in this section.

A. Inner ADRC Strategy for GFI Control

In this section, an inner ADRC is designed for the GFI system model presented in (12). Initially, injected currents i_g^{dq} are measured at PCC using three different current sensors and converted to i_g^{dq} through $abc \rightarrow dq$ transformation by using an estimated grid phase angle $\hat{\theta}_g$. The estimation of $\hat{\theta}_g$ is explained in the latter part of this section.

1) Inner ADRC Design: Based on i_g^{dq}, the internal state variables $\{x_1^{dq}, x_2^{dq}, x_3^{dq}\}$ of this fourth-order perturbed system are further evaluated using RESO. The extended state variable x_4^{dq} corresponds to the lumped unknown disturbance ψ^{dq}. The purpose here is to control i_g^{dq} through the control input s_i^{dq}, where b_0 is the calculated input gain based on the LCL parameters. Consider $\varepsilon_g^{dq} (= x_1^{dq} - \hat{x}_1^{dq})$ as a small steady-state error while tracking the estimated state variable $\hat{x}_1^{dq}$ with the actual state variable
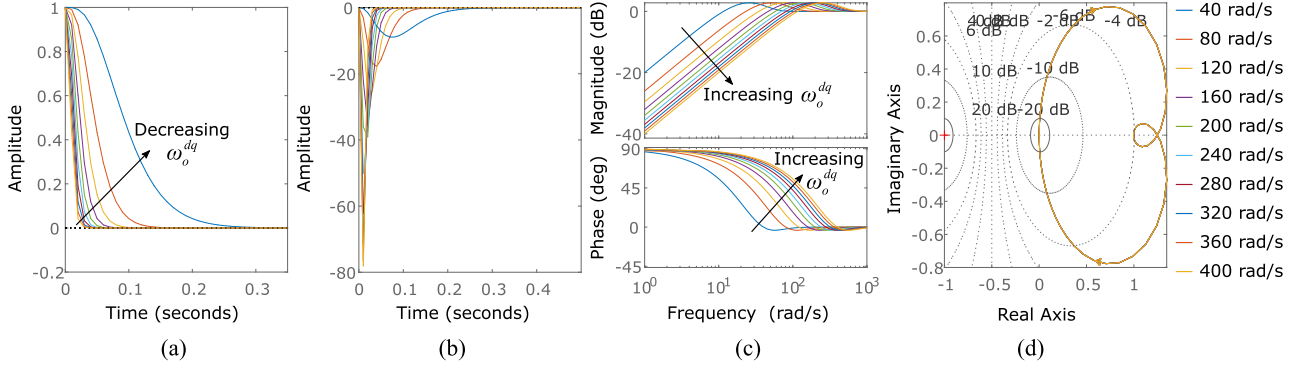
Fig. 4. Time and frequency domain analysis of $\Phi_e^{dq}(s)$ for RESO of inner ADRC. (a) Step response. (b) Impulse response. (c) Bode plot. (d) Nyquist plot.
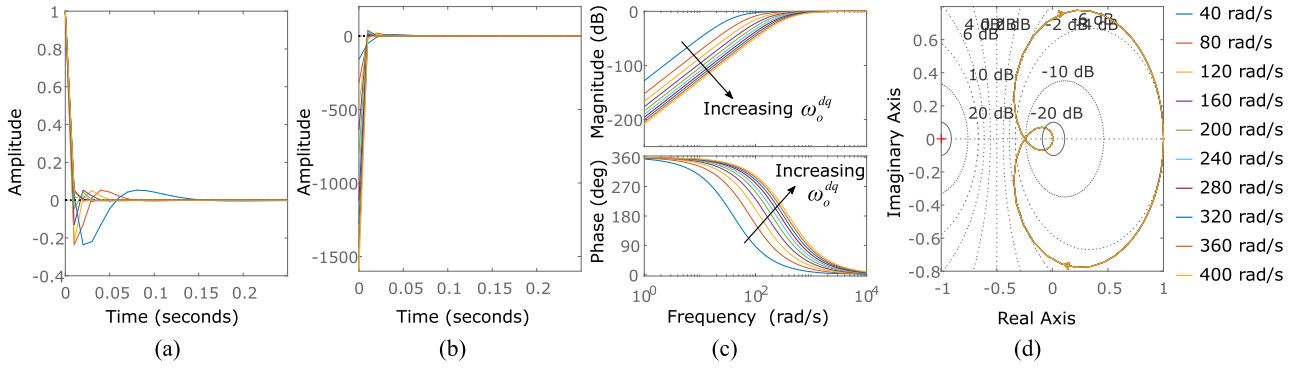

Fig. 5. Time and frequency domain analysis of $\Phi_e^{dq}(s)$ for PLLO of inner ADRC. (a) Step response. (b) Impulse response. (c) Bode plot. (d) Nyquist plot.
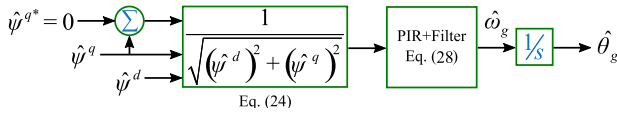

Fig. 6. Grid phase angle estimation method.

x_1^{dq} of the GFI system. Again, $[\hat{x}_1^{dq}, \hat{x}_2^{dq}, \hat{x}_3^{dq}] \rightarrow [x_1^{dq}, x_2^{dq}, x_3^{dq}]$ are the estimated state variables and $\hat{x}_4^{dq} \rightarrow x_4^{dq}$ is the estimated unknown external disturbance in dq-plane. As a consequence, the inner ADRC in the dq-plane can now be derived using the RESO and PLLO based external disturbance observer, as given in (19) and (20).

RESO design:

$$
\begin{cases}
\dot{\hat{x}}_1^{dq} = \hat{x}_2^{dq} + \beta_1^{dq}\varepsilon_g^{dq} \qquad \dot{\hat{x}}_2^{dq} = \hat{x}_3^{dq} + \beta_2^{dq}\varepsilon_g^{dq} \\
\dot{\hat{x}}_3^{dq} = \underbrace{-j\hat{\omega}_g\hat{x}_3^{dq} - \omega_r^2\hat{x}_2^{dq}}_{\text{Known disturbance estimation}} + b_0 s_i^{dq} + \hat{x}_4^{dq} + \beta_3^{dq}\varepsilon_g^{dq} \\
\dot{\hat{x}}_4^{dq} = \beta_4^{dq}\varepsilon_g^{dq} \\
\hat{y}_o^{dq} = \hat{x}_1^{dq}
\end{cases}
\tag{19}
$$

PLLO design:

$$
\begin{cases}
\dot{\hat{x}}_1^{dq} = \hat{x}_2^{dq} \qquad \dot{\hat{x}}_2^{dq} = \hat{x}_3^{dq} \\
\dot{\hat{x}}_3^{dq} = \underbrace{-j\hat{\omega}_g\hat{x}_3^{dq} - \omega_r^2\hat{x}_2^{dq}}_{\substack{\text{Known disturbance} \\ \text{estimation}}} + b_0 s_i^{dq} + \hat{x}_4^{dq} \\
\dot{\hat{x}}_4^{dq} = \beta_1^{dq}\dddot{\varepsilon}_g^{dq} + \beta_2^{dq}\ddot{\varepsilon}_g^{dq} + \beta_3^{dq}\dot{\varepsilon}_g^{dq} + \beta_4^{dq}\varepsilon_g^{dq} \\
\hat{y}_o^{dq} = \hat{x}_1^{dq}
\end{cases}
\tag{20}
$$

where $j = \left(\begin{bmatrix} 0 & 1 \\ -1 & 0 \end{bmatrix}\right)$ is the equivalent matrix form of the complex operator j defined previously and the superscript $[\,]^{dq}$ corresponds to a vector $[[\,]^d \, [\,]^q]^T$. The error margins and system stability criteria of the GFI system are used to define the observer gains $\{\beta_1^{dq}, \beta_2^{dq}, \beta_3^{dq}, \beta_4^{dq}\}$. Internal and external disturbances can be employed as feed-forward compensation terms for the GFI system control input, according to the ADRC theory mentioned in [8]. Consequently, it is possible to redefine the final control law of the GFI system, as given in (21).

$$
s_i^{dq} = s_{i0}^{dq} - b_0^{-1}\left(\hat{x}_4^{dq} - j\hat{\omega}_g\hat{x}_3^{dq} - \omega_r^2\hat{x}_2^{dq}\right)
\tag{21}
$$

where s_{i0}^{dq} is the initial value of the control input of the GFI system. Substituting (21), the perturbed system in (9) is reduced
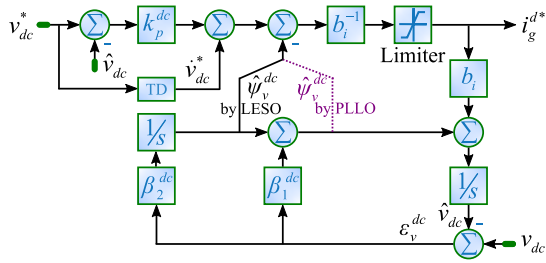
Fig. 7. Outer ADRC schematic with LESO (black dotted lines) and PLLO (pink dotted lines) implementation.

to (22).

$$\dot{x}_3^{dq} = b_0 s_{i0}^{dq} \tag{22}$$

2) Stability Analysis and Performance Tracking: With a simple proportional current controller given by (23), the desired inner closed-loop performance can be ascertained.

$$s_{i0}^{dq} = k_p^{dq}\left(i_g^{dq*} - i_g^{dq}\right) \tag{23}$$

where the proportional gain k_p^{dq} is selected as a trade-off between steady state and transient performance. The transfer function corresponding to the estimated disturbance $\hat{\psi}^{dq}$ and the actual disturbance ψ^{dq} is defined in (24).

$$\frac{\hat{\psi}^{dq}(s)}{\psi^{dq}(s)} = \begin{cases} \frac{\beta_4^{dq}}{s^4+\beta_1^{dq}s^3+\beta_2^{dq}s^2+\beta_3^{dq}s+\beta_4^{dq}} & \text{using RESO} \\ \frac{\beta_1^{dq}s^3+\beta_2^{dq}s^2+\beta_3^{dq}s+\beta_4^{dq}}{s^4+\beta_1^{dq}s^3+\beta_2^{dq}s^2+\beta_3^{dq}s+\beta_4^{dq}} & \text{using PLLO} \end{cases} \tag{24}$$

Here, the characteristics polynomial $(s^4 + \beta_1^{dq}s^3 + \beta_2^{dq}s^2 + \beta_3^{dq}s + \beta_4^{dq})$ is equated with the fourth-order undamped system $((s + \omega_o^{dq})^4)$ to estimate the observer gains β_1^{dq}, β_2^{dq}, β_3^{dq}, & β_4^{dq} as in (25). Based on this parameterization, all eigenvalues of observers are assigned to the undamped natural frequency (ω_o^{dq}) of the inner ADRC. The stability of the inner ADRC is tested at an observer bandwidth of $0.435\omega_o^{dq}$.

$$\beta_1^{dq} = 4\omega_o^{dq}, \quad \beta_2^{dq} = 6\left(\omega_o^{dq}\right)^2,$$
$$\beta_3^{dq} = 4\left(\omega_o^{dq}\right)^3, \quad \text{and} \quad \beta_4^{dq} = \left(\omega_o^{dq}\right)^4 \tag{25}$$

For the steady state response of the inner ADRC, the error transfer function of the disturbance may be used as in (26).

$$\Phi_e^{dq}(s) = \frac{\hat{\psi}_e^{dq}(s)}{\psi^{dq}(s)} = \frac{\psi^{dq}(s) - \hat{\psi}^{dq}(s)}{\psi^{dq}(s)}$$
$$= \begin{cases} \frac{s\left(s^3+\beta_1^{dq}s^2+\beta_2^{dq}s+\beta_3^{dq}\right)}{s^4+\beta_1^{dq}s^3+\beta_2^{dq}s^2+\beta_3^{dq}s+\beta_4^{dq}} & \text{using RESO} \\ \frac{s^4}{s^4+\beta_1^{dq}s^3+\beta_2^{dq}s^2+\beta_3^{dq}s+\beta_4^{dq}} & \text{using PLLO} \end{cases} \tag{26}$$

Adequate bandwidth in the RESO ensures a rapid response to disturbance variance, as seen in Figs. 4 and 5. Increasing the RESO/PLLO bandwidth results in higher overshoot, making it more susceptible to disturbances and uncertainties but with faster error settling. Comparing RESO and PLLO reveals that PLLO settles error dynamics more quickly. This can be observed from the time-domain analysis of step and impulse responses

for LESO (PLLO) in Figs. 4(a), (b), 5(a), and 5(b). These observations aid in selecting the ADRC bandwidth considering the steady-state error. In comparison to RESO, PLLO achieves the desired performance with approximately $1/6^{th}$ of RESO's bandwidth. However, PLLO exhibits a greater overshoot. Consequently, a trade-off must be made between bandwidth and overshoot. Ultimately, bandwidths of 100 rad/s (PLLO) and 300 rad/s (RESO) are chosen. The parameter k_p^{dq}, selected between 20% and 33% of ω_o^{dq}, enhances ADRC's current performance, provided settling time specifications for transient response are considered. Frequency domain analysis (Bode plot) in Figs. 4(c) and 5(c) reveals that increasing bandwidth does not significantly improve ADRC performance for either RESO or PLLO. PLLO has a phase margin of $-180°$, while RESO exhibits a phase margin of $-129.69°$. PLLO's resonant peak is higher than RESO's. The Nyquist plots, shown in Figs. 4(d) and 5(d), indicate the open-loop performance of RESO and PLLO, with bandwidths not greatly impacting ADRC's open-loop stability. As bandwidth increases, disturbance estimation errors decrease, and tracking speed increases.

3) Grid Frequency and Phase Angle Estimation: This section presents an estimation method for the phase and frequency of the grid voltage. Fig. 6 exhibits such estimation process in dq-plane. To accurately estimate the q-axis unknown external disturbance state $\hat{\psi}_e^q$, the grid voltage phase error information $\hat{\psi}^{dq}$ $(=\hat{\psi}^d + j\hat{\psi}^q)$ must be normalized as given in (27). Equation (27) also indicates that $\hat{\psi}_e^q$ depends on change in fundamental grid angular frequency $(\Delta\omega_g)$, the normalized angular frequency amplitude $(\Omega_{n\pm3\hbar})$ and corresponding phase $(\theta_{\pm3\hbar})$ of the $(\pm3\hbar)th$ grid voltage harmonic.

$$\hat{\psi}_e^q = \frac{\hat{\psi}^{q*} - \hat{\psi}^q}{\sqrt{\left(\hat{\psi}^d\right)^2 + \left(\hat{\psi}^q\right)^2}}$$
$$= \Delta\omega_g \pm \sum_{\hbar=1}^{n} \Omega_{n\pm3\hbar} \sin\begin{pmatrix} \pm3\hbar\omega_g t \\ +\theta_{\pm3\hbar} \end{pmatrix} \tag{27}$$

Harmonic content in $\hat{\psi}_e^q$ must be suppressed to obtain $\hat{\omega}_g$ by using a proportional integral resonant (PIR) tracking controller with a low-bandwidth loop filter to bring the normalized $\hat{\psi}^q$ to zero. As demonstrated in Fig. 6, the transfer function of these tracking controller assemblies is obtained as shown in (28).

$$G_\omega(s) = \left(k_p + \frac{k_i}{s} + k_r \frac{k_d\frac{\omega_{rc}}{Q_d}s}{s^2 + k_d\frac{\omega_{rc}}{Q_d}s + \omega_{rc}^2}\right)\left(\frac{\omega_c}{s + \omega_c}\right) \tag{28}$$

where k_p, k_i, k_r and k_d are the proportional, integral, resonant gain, and damped gain of the PIR controller, respectively. The quality factor of the damped term of the resonant controller is denoted by Q_d. The PIR controller achieves a desirable steady-state value of $\hat{\omega}_g$ with minimized steady-state error, but it struggles to track the angular frequency of the grid with high accuracy. To counteract the effects of LCL filter resonance on tracking $\hat{\omega}_g$, a resonant term is added to the existing PI controller in (28). The resonant controller's angular frequency (ω_{rc}) is set to twice the nominal grid angular frequency $(\omega_{gn}$, i.e., $2\pi f_{gn})$, or $\omega_{rc} = 2\omega_{gn}$, without affecting the high-frequency stability
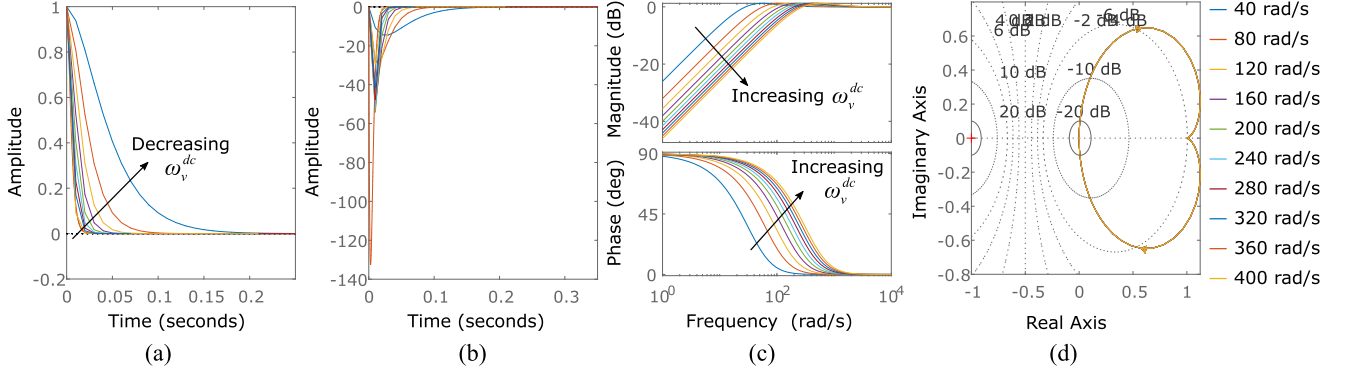
Fig. 8. Time and frequency domain analysis for $\Phi_v^{dc}(s)$ using LESO of outer ADRC. (a) Step response. (b) Impulse response. (c) Bode plot. (d) Nyquist plot.
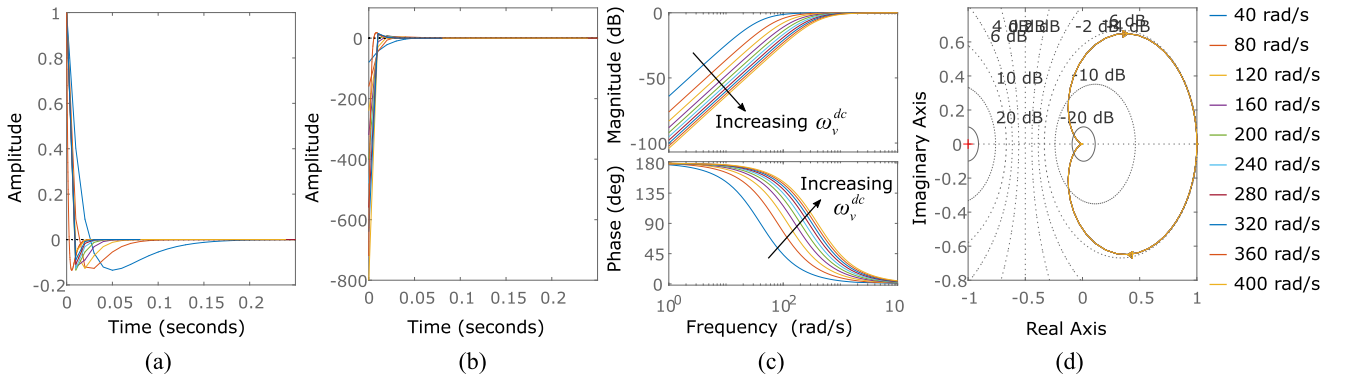

Fig. 9. Time and frequency domain analysis for $\Phi_v^{dc}(s)$ using PLLO of outer ADRC. (a) Step response. (b) Impulse response. (c) Bode plot. (d) Nyquist plot.

of the GFI system; here, the grid's nominal frequency f_{gn} is considered as 50 Hz, and a damping term is added to the traditional resonant controller to avoid instability due to grid frequency variation and discretization errors.

The linear dynamic response of the PIR tracking controller to predicted disturbances can accommodate any fundamental operating frequency. The proposed estimation approach, which employs a dq reference frame instead of a stationary $\alpha\beta$ frame, is less complex than PLL-based grid voltage phase estimation, as it avoids the need for a low pass filter and phase delay associated with intricate cut-off frequency selection [24]. A stable closed-loop transfer function of the PIR tracking controller can be achieved with the necessary and sufficient criteria of $\omega_c + k_p > 0$, allowing k_i to be set to 20 Hz and enabling filter bandwidth adjustment via k_p. The low-pass filter cutoff frequency (ω_c) is set to five times the value of ω_{gn}, and the grid phase angle can be estimated as given in (29).

$$\hat{\theta}_g = \int \hat{\omega}_g dt. \tag{29}$$

B. Outer ADRC Strategy for DC-Link Voltage Control

1) Outer ADRC Design: The perturbed first-order system in (18) includes feedback from the estimated $\hat{v}_{dc}$ and measurement noise δ_n. The DC-link voltage controller can be designed as an

external disturbance observer utilizing a LESO or PLLO-based observer, as described in (30) and (31). Here, $[\hat{v}_{dc}, \hat{\psi}_v^{dc}] \rightarrow [v_{dc}, \psi_v^{dc}]$, are the estimated value of the DC-link voltage and unknown total disturbances, $\varepsilon_v^{dc} = v_{dc} - \hat{v}_{dc}$ is the DC-link voltage error.

LESO design:

$$\begin{cases} \dot{\hat{v}}_{dc} = b_i i_g^{d*} + \hat{\psi}_v^{dc} + \beta_1^{dc}\varepsilon_v^{dc}; & \dot{\hat{\psi}}_v^{dc} = \beta_2^{dc}\varepsilon_v^{dc} \end{cases} \tag{30}$$

PLLO design:

$$\begin{cases} \dot{\hat{v}}_{dc} = b_i i_g^{d*} + \hat{\psi}_v^{dc}; & \dot{\hat{\psi}}_v^{dc} = \beta_1^{dc}\dot{\varepsilon}_v^{dc} + \beta_2^{dc}\varepsilon_v^{dc} \end{cases} \tag{31}$$

2) Stability and Tracking performance Analysis: When LESO/PLLO given in (30)–(31) is stable, the estimation error ε_v^{dc} converges to zero. Let ε_e^{dc} be the DC-link voltage tracking error and can be defined as $\varepsilon_e^{dc} = v_{dc}^* - \hat{v}_{dc}$. The DC-link voltage tracking error dynamics can be represented as (32) by utilizing (31).

$$\dot{\varepsilon}_e^{dc} = \dot{v}_{dc}^* - \dot{\hat{v}}_{dc} = \dot{v}_{dc}^* - \left(b_i i_g^{d*} + \hat{\psi}_v^{dc}\right) \tag{32}$$

In order to track the reference DC-link voltage (v_{dc}^*), an appropriate linear feedback control law is implemented in (33).

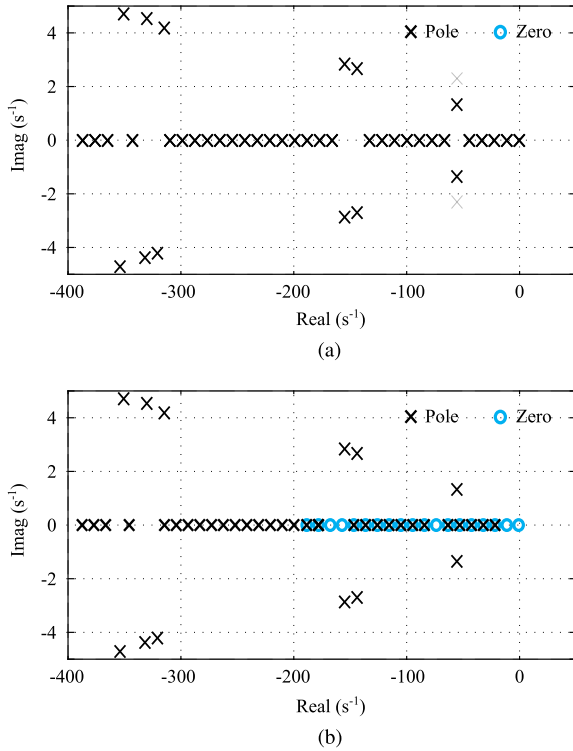$$\dot{\varepsilon}_e^{dc} = -k_p^{dc}\varepsilon_e^{dc} = -k_p^{dc}\left(v_{dc}^* - \hat{v}_{dc}\right) \tag{33}$$
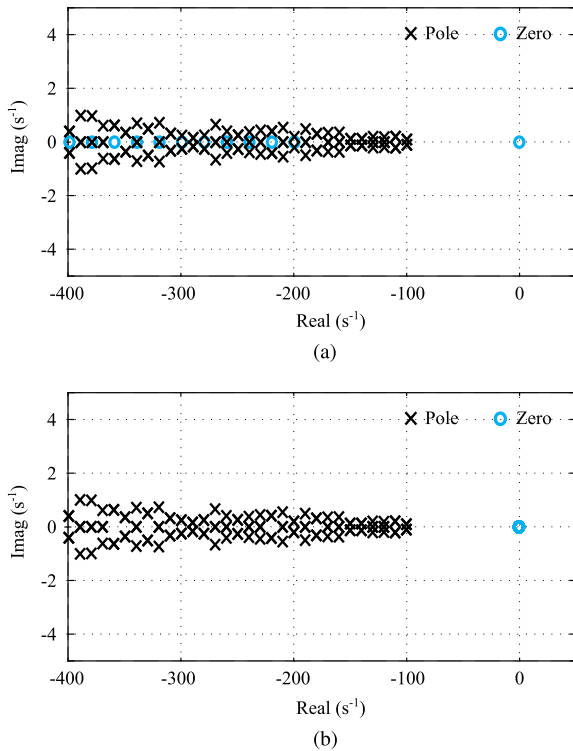
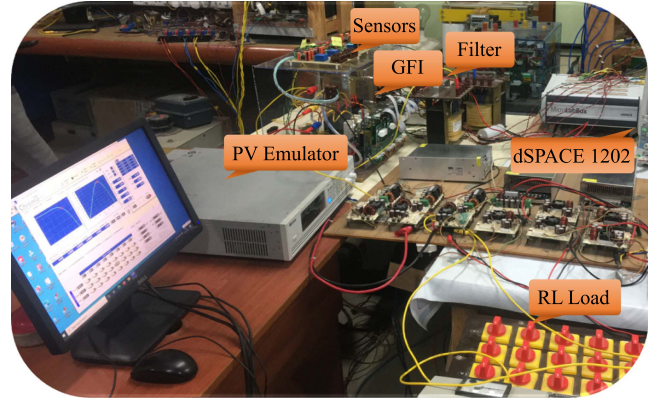Fig. 10. Stability analysis for outer loop controller though pole-zero plot. (a) For LESO. (b) For PLLO.

Fig. 12. Hardware prototype for photovoltaics GFI system.

where k_p^{dc} denotes the proportional gain of the outer ADRC DC-link voltage regulator, as shown in Fig. 7. Equation (34) represents the final control law of the outer ADRC by solving (32) and (33).

$$i_g^{d*} = b_i^{-1} \left[i_{g0}^{d*} + \dot{v}_{dc}^* - \hat{\psi}_v^{dc} \right] \tag{34}$$

where $i_{g0}^{d*} (= k_p^{dc}(v_{dc}^* - \hat{v}_{dc}))$ is considered as the initial value of the control input of the PV system. The derivative term $\dot{v}_{dc}^*$ serves as a feedforward term that tracks the variation in reference speed to reduce oscillation and overshoot during speed adjustment. $\dot{v}_{dc}^*$ can be generated by using a tracking differentiator (TD). By considering $\hat{v}_{dc}$ as the DC-link voltage feedback, the closed-loop transfer function of the DC-Link controller can be expressed as (35).

$$\frac{v_{dc}(s)}{v_{dc}^*(s)} = \frac{b_i k_p^{dc}}{s + b_i k_p^{dc}} \tag{35}$$

The outer ADRC must be able to accurately track external disturbance during grid power injection. Eq. (36) represents the transfer function corresponding to the estimated value $\hat{\psi}_v^{dc}(s)$ and the actual value $\psi_v^{dc}(s)$ of the external disturbance that affects the voltage of the DC-link.

$$\Phi_v^{dc}(s) = \frac{\hat{\psi}_v^{dc}(s)}{\psi_v^{dc}(s)} = \begin{cases} \frac{\beta_2^{dc}}{s^2 + \beta_1^{dc} s + \beta_2^{dc}} & \text{using LESO} \\ \frac{\beta_1^{dc} s + \beta_2^{dc}}{s^2 + \beta_1^{dc} s + \beta_2^{dc}} & \text{using PLLO} \end{cases} \tag{36}$$

where β_1^{dc} and β_2^{dc} can be chosen from the characteristic polynomial of LESO/PLLO i.e. $s^2 + \beta_1^{dc} s + \beta_2^{dc} = (s + \omega_v^{dc})^2$. Consider ω_v^{dc} as the undamped natural frequency of the outer voltage control loop. Now, through equating the above relation, $\beta_1^{dc} = 2\omega_v^{dc}$ and $\beta_2^{dc} = (\omega_v^{dc})^2$ can be obtained. The stability of the outer ADRC with LESO and PLLO can be achieved with ω_v^{dc} varies from $40\,rad/s$ to $400\,rad/s$ with an incremental value of $40\,rad/s$, which can be seen from Figs. 8 and 9. The outer ADRC performance with LESO (PLLO) is evaluated from Fig. 8 (Fig. 9), which assists in selecting bandwidth based on settling time and resonant peak. This evaluation is conducted similarly to the approach in Section III-A2. Fig. 8(c) and (d) (Fig. 9(c) and (d)) present the Bode Diagram and Nyquist plot for LESO

Fig. 11. Stability analysis for inner loop controller though pole-zero plot. (a) For RESO. (b) For PLLO.

TABLE I
SYSTEM PARAMETERS

PV system parameters
Maximum p_{pv}=7.9 kW, Open circuit voltage (v_{oc})=86.5 V, Short circuit current (i_{sc})=6.5 A, Maximum v_{pv}=72.9 V, Maximum i_{pv}=6.04 A, Maximum power per panel=440.36 W, Number of series (N_{se}) and parallel panels (N_p)=9 and 2
GFI system parameters
Grid voltage at PCC and frequency (V_g, f_g)=230 V, 50 Hz, C_{dc}=2200 μF, L_g=1.4 mH, L_i=1.7 mH, C_f=50 μF, r_g=0.1 Ω, r_i=0.4 Ω, Grid impedance (Z_g)= 0.01+j0.047 Ω, Switching frequency (f_{sw})= 10 kHz

(PLLO) to analyze disturbance rejection and noise suppression in the outer ADRC. When LESO and PLLO are employed together, the outer ADRC performance of PLLO surpasses that of LESO if noise suppression characteristics are comparable.

Stability analysis of the proposed techniques is studied through pole-zero plots with assumptions that the inner loop control is ideal with a short settling time, no transients, and non-linearities are ignored. Under these assumptions, the inner loop is considered to have unity gain for outer loop controller analysis [25]. The pole-zero plot in Fig. 10 shows stability analysis for outer loop controller using LESO and PLLO approaches. For both approaches, all poles lie on the left half of the s-plane, indicating system stability. System zeros may exist due to the error transfer function study, but they don't influence stability, only affecting settling time and overshoot. When studying inner-loop ADRC with RESO and PLLO methods individually, all poles also lie on the left-hand side of the s-plane, as shown in Fig. 11, confirming system stability.

IV. RESULTS AND DISCUSSIONS

A. Prototype Description

The effectiveness of the proposed ADRC is validated on a single-state PV-GFI laboratory experimental prototype, as shown in Fig. 12. The system parameter descriptions are provided in Table I. The PV-GFI prototype includes a voltage source inverter, a PV emulator, current sensors, voltage sensors, a rectifier with RL load, and a dSPACE MicroLabBox DS1202. The DSP controller DS1202 is utilized for digital pulse generation to control the GFI. The signals from current and voltage sensors are given as feedback to DS1202 through the internal ADCs. The sampling time of the DS1202 is set to 50 μs.

B. Experimental Verification Through Test Scenarios

The performance of the proposed ADRC controller is examined in five different scenarios are listed below.
- Scenario-1: Sudden change in solar irradiance.
- Scenario-2: Sudden change in solar temperature.
- Scenario-3: Filter parameter variation.
- Scenario-4: Grid voltage is subjected to voltage sag.
- Scenario-5: Grid voltage is subjected to phase jump.
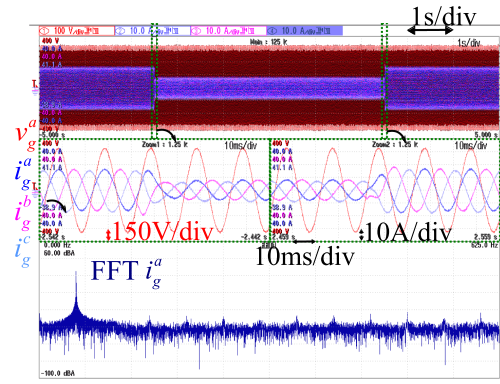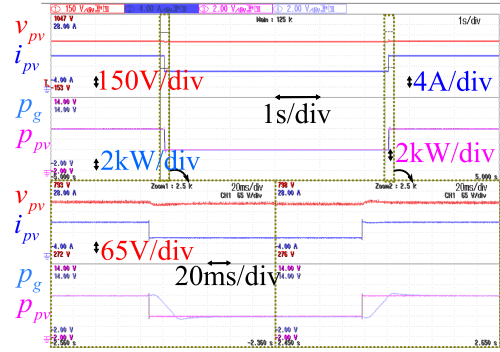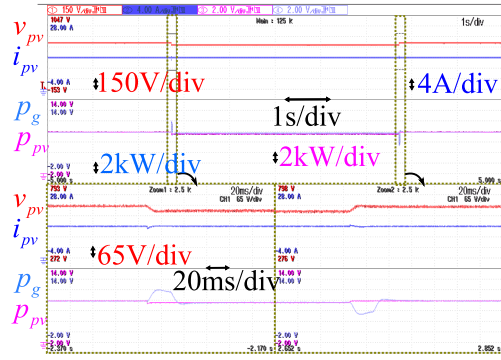

Fig. 13. Experimental results under Scenario-1. (a) v_g^a, i_g^a, i_g^b, and i_g^c. (b) v_{pv}, i_{pv}, p_g, and p_{pv}.

1) Scenario-1: Fig. 13 shows the experimental results for the three-phase GFI based on the proposed ADRC controller in Scenario-1. In Scenario 1, the dynamic change in solar irradiance can be observed from 1000 W/m^2 to 500 W/m^2 and 500 W/m^2 to 1000 W/m^2. The solar temperature is kept constant at 25 °C during this irradiance change. The performance of phase voltage v_g^a and three-phase grid current i_g^a, i_g^b, i_g^c are shown in Fig. 13(a). It can be seen that v_g^a and i_g^a are in phase, which indicates that the system can maintain the unity power factor in scenario 1. Fig. 13(a) (bottom) represents a zoomed portion of v_g^a, i_g^a, i_g^b, and i_g^c waveforms during the sudden change of solar irradiance. It can be seen that the grid current is sinusoidal in nature. Moreover, the THD of i_g^a is kept within the limit of the IEEE-519 standard. The PV voltage v_{pv}, the PV current i_{pv}, the PV power p_{pv} and grid active power p_g can be shown in Fig. 13(b). It can be observed that a small change in v_{pv} occurs during this scenario-1, which tracks the reference MPPT voltage generated by P & O algorithm. Due to a sudden change in irradiance from 1000 W/m^2 to 500 W/m^2, i_{pv} falls from $12A$ to $6A$. Moreover, the injected grid active power is 7.86 kW and 3.86 kW for 1000 W/m^2 and 500 W/m^2 irradiance, respectively.

2) Scenario-2: Fig. 14 shows the experimental results for proposed ADRC controller based three-phase grid inverter under Scenario-2. At constant 1000 W/m^2 irradiance, the dynamic change in solar temperature from 25 °C to 35 °C and 35 °C to 25 °C can be observed in this Scenario-2. Fig. 14(a) depicts the performance of v_g^a, i_g^a, i_g^b, and i_g^c during a rapid temperature
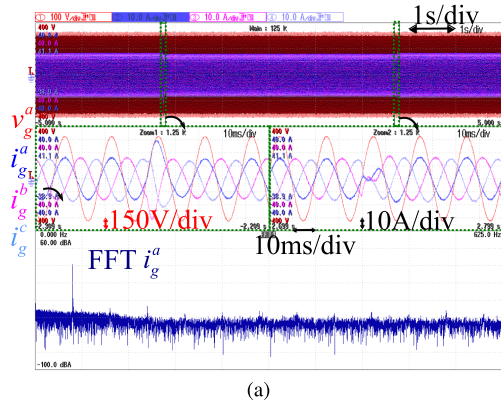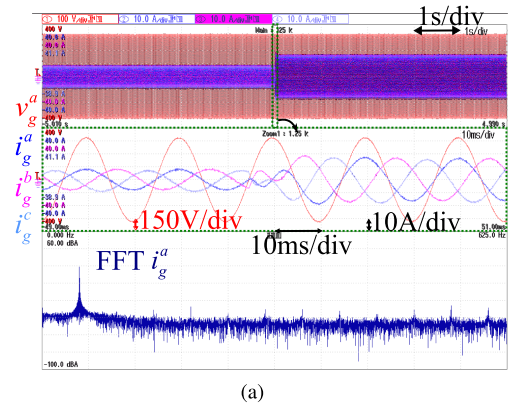
(a)

(b)

Fig. 14. Experimental results under Scenario-2. (a) v_g^a, i_g^a, i_g^b, and i_g^c. (b) v_{pv}, i_{pv}, p_g, and p_{pv}.

(a)

(b)

Fig. 15. Experimental results under Scenario-3. (a) v_g^a, i_g^a, i_g^b, and i_g^c. (b) v_{pv}, i_{pv}, p_g, and p_{pv}.
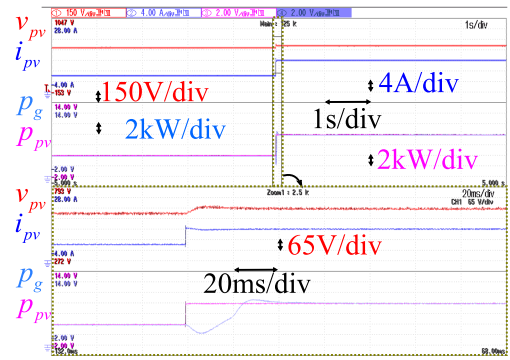
change. It can be observed that when the temperature increases, the grid current falls and vice versa. Furthermore, the THD of i_g^a is 2%, indicating that it is within the IEEE-519 standard. The v_g^a and i_g^a are kept at unity power factor. During a fast change in temperature, a small change occurs in i_{pv} as shown in Fig. 14(b). In addition, v_{pv} track the reference MPPT voltage. v_{pv} decreases from 658 V to 631 V due to a rapid change in temperature from 25 °C to 35 °C. Moreover, the injected grid active power is 7.86 kW for 25 °C and 7.54 kW for 35 °C temperature.

3) Scenario-3: The robustness of the proposed ADRC controller-based three-phase grid inverter is observed under +10% change in filter parameters, as shown in Fig. 15. Simultaneously, solar irradiation changes from 500 W/m² to 1000 W/m². It can be seen in Fig. 15(a) that solar irradiation increases as the grid current increases and maintains in sinusoidal in nature. The THD of i_g^a is kept within the limit of the IEEE-519 standard. In Fig. 15(b), v_{pv} change from 649 V to 650 V and i_{pv} change from 6 A to 12 A at 500 W/m² to 1000 W/m². The PV voltage, v_{pv} maintains stable and tracks the maximum voltage during this Scenario-3. Moreover, the active grid power injects maximum power into the grid.

4) Scenario-4: Fig. 16 illustrates the experimental results during the balance grid voltage sag condition. The grid voltage with 20% voltage sag is illustrated in Fig. 16(a). The system is operated in a constant power region, which increases the grid current i_g^a, i_g^b, i_g^c under voltage sag condition. During this voltage

sag, the % THD of the grid currents are observed to be 1.68%. It can be observed from Fig. 16(b), there is no effect on v_{pv}, i_{pv} and p_{pv} during the voltage sag condition. It indicates that v_{pv} remains stable during this Scenario-4. In addition, the active power of the injected grid tracks the maximum power of the PV array.

5) Scenario-5: The performance analysis under Scenario-5 is shown in Fig. 17, which is depicted from the experimental evaluation. This scenario-5 considers the grid voltage with a 60° phase jump, as indicated in Fig. 17(a). During this phase jump scenario, the grid currents i_g^a, i_g^b, and i_g^c return to normal condition after a few cycles. As seen in Fig. 17, there is no influence on v_{pv}, i_{pv} and p_{pv} throughout this scenario, which indicates that v_{pv} is stable. Furthermore, the injected grid active power is obtained as the maximum power of the PV array.

C. Comparative Analysis

In scenarios 4 and 5, the proposed inner ADRC approach is compared to ADRC-[9]. In ADRC-[9], the fixed DC-link voltage is employed as an input source to analyze the performance of the grid scenario. To offer a fair comparison with the proposed controller, the input voltage of ADRC-[9] is linked to the PV array. Furthermore, both current-controller approaches are combined with the same outer-loop controller. Figs. 16 and 17 depict the performance of both current controller techniques under Scenarios 4 and 5, respectively. It can be shown from Fig. 16(b)
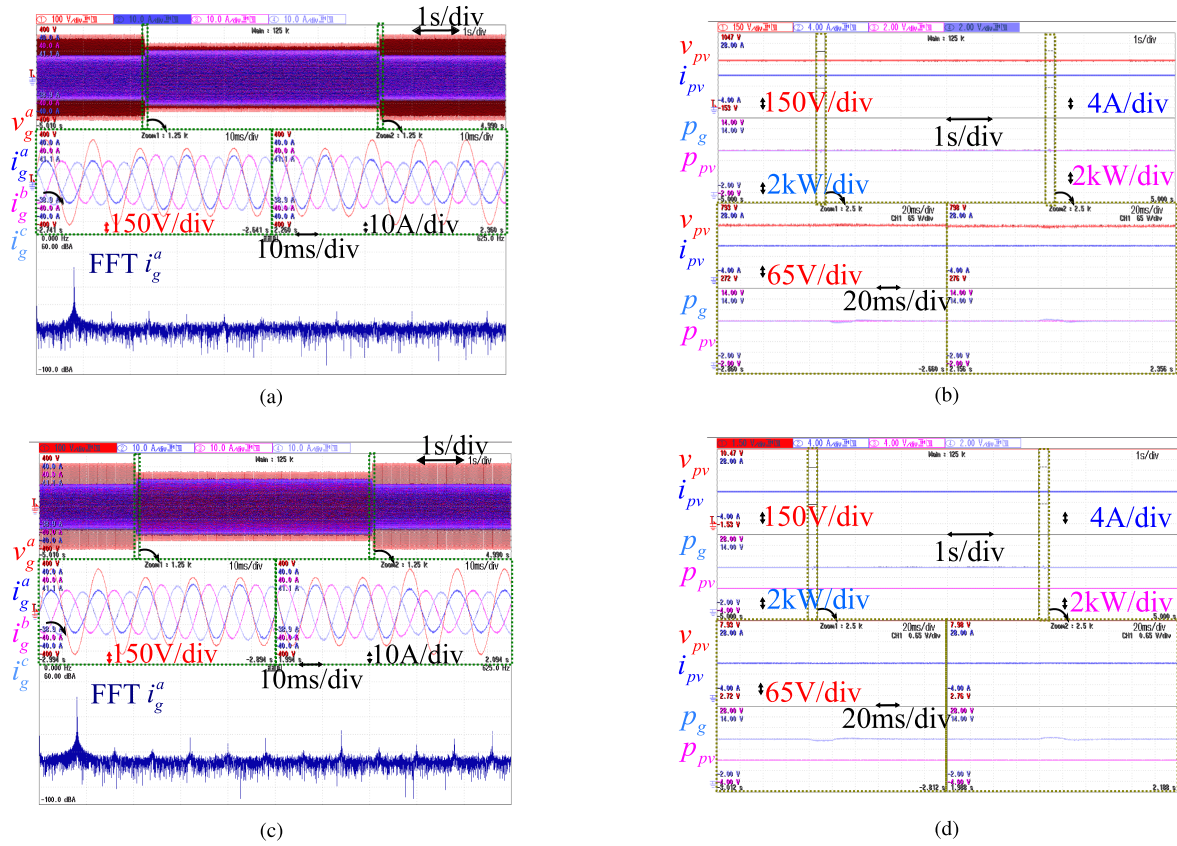
Fig. 16. Experimental results with comparative study under Scenario-4. (a) v_g^a, i_g^a, i_g^b, and i_g^c results with proposed ADRC. (b) v_{pv}, i_{pv}, p_g, and p_{pv} results with proposed ADRC. (c) v_g^a, i_g^a, i_g^b, and i_g^c results with proposed ADRC- [9]. (d) v_{pv}, i_{pv}, p_g, and p_{pv} results with proposed ADRC- [9].

TABLE II
COMPARISON BETWEEN THE PROPOSED ADRC METHOD AND CONVENTIONAL
PI CONTROLLER FOR DC LINK ERROR SIGNAL

Test scenario	Proposed ADRC method	PI controller [3]
Solar irradiation $(1000-500W/m^2)$	$t_s=50, \epsilon_m=6.7$	$t_s=160, \epsilon_m=8.1$
Solar temperature $(35-25°C)$	$t_s=56, \epsilon_m=3.3$	$t_s=60, \epsilon_m=3.4$
0.2 pu Voltage sag	$t_s=60, \epsilon_m=3$	$t_s=85, \epsilon_m=4.69$
60° Phase angle jump	$t_s=75, \epsilon_m=3$	$t_s=70, \epsilon_m=6$

Note: Settling time: t_s (ms), peak overshoot error: ϵ_m (V)

TABLE III
COMPARISON BETWEEN PROPOSED ESTIMATION METHOD AND
MSTOGI-PLL-[26]

Test scenario	Proposed Method	MSTOGI-PLL-[26]
0.2 pu Voltage sag	$t_s=60, \epsilon_f=3.6$	$t_s=95, \epsilon_f=5$
60° Phase angle jump	$t_s=65, \epsilon_f=28$	$t_s=110, \epsilon_f=25$

Note: Settling time: t_s (ms), frequency overshoot: ϵ_f (Hz)

ADRC with standard PI controllers in the presence of various disturbances of the grid. The proposed ADRC techniques have a faster dynamic response than the traditional PI controller under 0.2 pu voltage sag, changes in solar irradiation, and temperature. Furthermore, for various disturbances in the grid, the suggested approach exhibits a lower peak overshoot error than the typical PI controller.

As demonstrated in the Fig. 20 , performances of the estimated frequency and phase angle of the proposed technique are compared with MSTOGI-PLL-[26]. In this analysis, the grid voltage is subjected to a 0.2 pu voltage sag and a 60° phase angle jump. Table III displays the results of the proposed techniques and MSTOGI-PLL-[26]. Under the 0.2 pu voltage sag, 60° phase angle jump, the proposed techniques provide a quicker transient response with less settling time than MSTOGI-PLL-[26].

and (d) in Scenario-4 that the performance on the input side is identical, which has no influence on v_{pv}, i_{pv} and p_{pv}. According to Fig. 16(a) and (c), the %THD of i_g^a using the proposed inner ADRC controller and ADRC-[9] are 1.68% and 2.48%, respectively. Similarly, %THD of i_g^a with the proposed inner ADRC controller and the ADRC-RESO technique mentioned [9] in Fig. 17(a) and (c) in Scenario-5 are 2% and 2.78%, respectively. Figs. 18 and 19 shows a performance comparison of the proposed ADRC and traditional PI controller [3] for the DC link under input side scenario and grid side conditions, respectively. Table II compares the effectiveness of the proposed
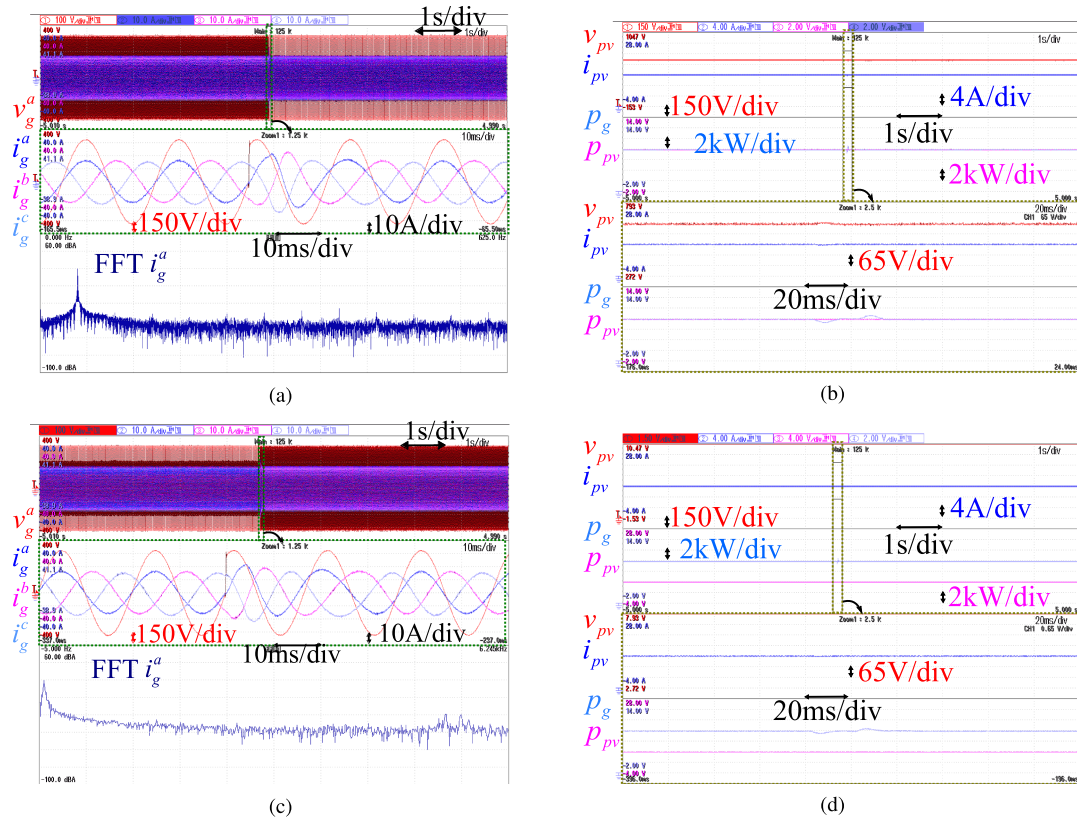
(a)

(b)

(c)

(d)

Fig. 17. Experimental results with comparative study under Scenario-5. (a) v_g^a, i_g^a, i_g^b, and i_g^c results with proposed ADRC. (b) v_{pv}, i_{pv}, p_g, and p_{pv} results with proposed ADRC. (c) v_g^a, i_g^a, i_g^b, and i_g^c results with proposed ADRC-[9]. (d) v_{pv}, i_{pv}, p_g, and p_{pv} results with proposed ADRC-[9].
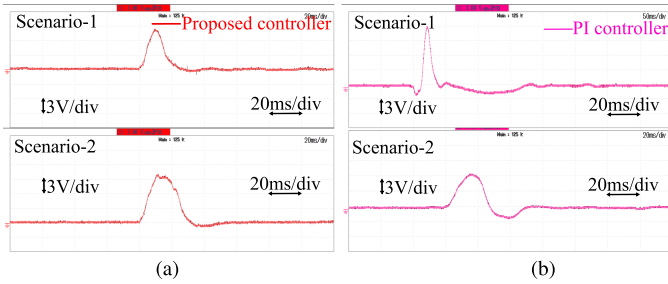

(a)

(b)

Fig. 18. Results of dc-link voltage error signal under scenarios 1 and 2. (a) Proposed ADRC method. (b) PI controller [3].
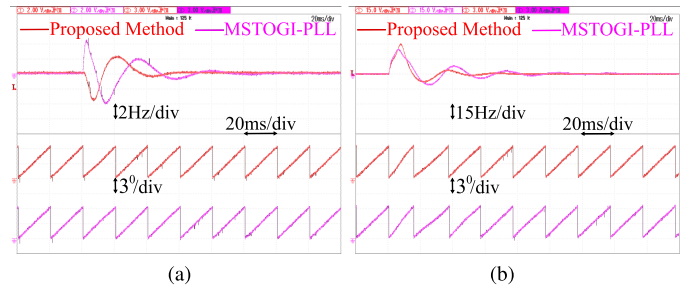

(a)

(b)

Fig. 20. Experimental comparative analysis of the proposed method with [26] for frequency and phase error estimation. (a) During voltage sag. (b) During phase jump.

(a)

(b)
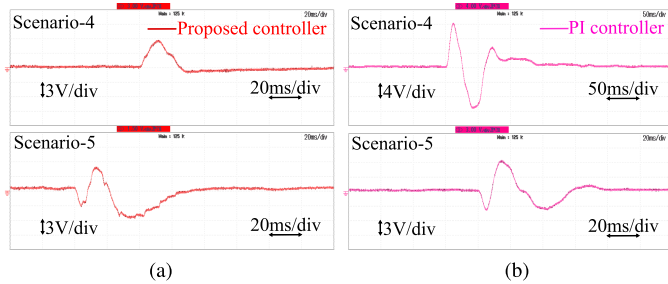
Fig. 19. Experimental results of dc-link error signal under scenarios 4 and 5. (a) With proposed ADRC. (b) Comparing with PI controller [3].

V. CONCLUSION

This paper presents an initial model of the PV-GFI system with LCL filter, taking into account the system parameter uncertainties and unknown grid disturbances. The current inner loop is decoupled in the dq-domain via detecting disturbances and then applying RESO/PLLO for the implementation of inner loop ADRCs. With the use of discrete-time frequency analysis and pole-zero maps, the suggested inner ADRCs have been shown to be robust and stable under internal uncertainties. Through the use of this internally generated disturbance, the grid voltage and frequency phase angles are determined without the use of

an external PLL. To control the DC-link voltage, a combination of the LESO and PLLO with the suggested outer ADRC is examined, taking into account the uncertainties relating to photovoltaics and grid voltages. Under Various disturbances and uncertainties, the proposed ADRC systems demonstrate their feasibility and effectiveness. It can be observed that the proposed decoupling control strategy requires a lesser number of sensors, insensitive to control settings, and highly resilient. Furthermore, it is likely to significantly improve the quality of grid-side current.

REFERENCES

[1] Y. Han et al., "Modeling and stability analysis of LCL-type grid-connected inverters: A comprehensive overview," *IEEE Access*, vol. 7, pp. 114975–115001, 2019.

[2] S. Bacha, D. Picault, B. Burger, I. Etxeberria-Otadui, and J. Martins, "Photovoltaics in microgrids: An overview of grid integration and energy management aspects," *IEEE Ind. Electron. Mag.*, vol. 9, no. 1, pp. 33–46, Mar. 2015.

[3] M. Rezkallah, S. K. Sharma, A. Chandra, B. Singh, and D. R. Rousse, "Lyapunov function and sliding mode control approach for the solar-PV grid interface system," *IEEE Trans. Ind. Electron.*, vol. 64, no. 1, pp. 785–795, Jan. 2017.

[4] A. Benrabah, D. Xu, and Z. Gao, "Active disturbance rejection control of LCL-filtered grid-connected inverter using padé approximation," *IEEE Trans. Ind. Appl.*, vol. 54, no. 6, pp. 6179–6189, Nov. 2018.

[5] S. Das and B. Subudhi, "A two-degree-of-freedom internal model-based active disturbance rejection controller for a wind energy conversion system," *IEEE Trans. Emerg. Sel. Topics Power Electron.*, vol. 8, no. 3, pp. 2664–2671, Sep. 2020.

[6] M. Wang, X. Wang, J. Qiao, and L. Wang, "Improved current decoupling method for robustness improvement of LCL-type STATCOM based on active disturbance rejection control," *IEEE Access*, vol. 7, pp. 121781–121792, 2019.

[7] H. Zhang, J. Xian, J. Shi, S. Wu, and Z. Ma, "High performance decoupling current control by linear extended state observer for three-phase grid-connected inverter with an LCL filter," *IEEE Access*, vol. 8, pp. 13119–13127, 2020.

[8] S. Ahmad and A. Ali, "Unified disturbance-estimation-based control and equivalence with IMC and PID: Case study on a DC—DC boost converter," *IEEE Trans. Ind. Electron.*, vol. 68, no. 6, pp. 5122–5132, Jun. 2021.

[9] T. V. Tran, K.-H. Kim, and J.-S. Lai, "Optimized active disturbance rejection control with resonant extended state observer for grid voltage sensorless LCL-filtered inverter," *IEEE Trans. Power Electron.*, vol. 36, no. 11, pp. 13317–13331, Nov. 2021.

[10] S. M. Hoseinizadeh, S. Ouni, H. Karimi, M. Karimi-Ghartemani, and K. L. Lian, "Comparison of PLL-based and PLL-less vector current controllers," *IEEE Trans. Emerg. Sel. Topics Power Electron.*, vol. 10, no. 1, pp. 436–445, Feb. 2022.

[11] S. Maganti and N. P. Padhy, "Analysis and design of PLL less current control for weak grid-tied LCL type voltage source converter," *IEEE Trans. Emerg. Sel. Topics Power Electron.*, vol. 10, no. 4, pp. 4026–4040, Aug. 2022.

[12] B. Zhang, X. Zhou, and Y. Ma, "Improved linear active disturbance rejection control of photovoltaic grid connected inverter based on filter function," *IEEE Access*, vol. 9, pp. 141725–141737, 2021.

[13] Y. Zhang et al., "Dynamic performance improving sliding-mode control-based feedback linearization for PV system under LVRT condition," *IEEE Trans. Power Electron.*, vol. 35, no. 11, pp. 11745–11757, Nov. 2020.

[14] X. Zhou, Q. Liu, Y. Ma, and B. Xie, "DC-link voltage research of photovoltaic grid-connected inverter using improved active disturbance rejection control," *IEEE Access*, vol. 9, pp. 9884–9894, 2021.

[15] J. Lu, S. Golestan, M. Savaghebi, J. C. Vasquez, J. M. Guerrero, and A. Marzabal, "An enhanced state observer for DC-link voltage control of three-phase AC/DC converters," *IEEE Trans. Power Electron.*, vol. 33, no. 2, pp. 936–942, Feb. 2018.

[16] Y. Cai, Y. He, H. Zhou, and J. Liu, "Active-damping disturbance-rejection control strategy of LCL grid-connected inverter based on inverter-side-current feedback," *IEEE Trans. Emerg. Sel. Topics Power Electron.*, vol. 9, no. 6, pp. 7183–7198, Dec. 2021.

[17] Y. Xiong, Y. Ye, Y. Cao, and Y. Wu, "Separate-structure UDE-based current resonant control strategy on LCL-type grid-tied inverters with weighted average current method for improved injected current quality and robustness," *IEEE Trans. Power Electron.*, vol. 35, no. 12, pp. 13641–13651, Dec. 2020.

[18] W. Ma, Y. Guan, B. Zhang, and L. Wu, "Active disturbance rejection control based single current feedback resonance damping strategy for LCL-type grid-connected inverter," *IEEE Trans. Energy Convers.*, vol. 36, no. 1, pp. 48–62, Mar. 2021.

[19] I. P. Nikolakakos, U. R. Muduli, M. S. El Moursi, K. Al Hosani, S. A. Mohamed, and T. Ghaoud, "An impedance-based stability analysis for constant power load with line failure," in *Proc. IEEE Power Energy Conf. Illinois*, 2022, pp. 1–6.

[20] S. Jayalath and M. Hanif, "Generalized LCL-filter design algorithm for grid-connected voltage-source inverter," *IEEE Trans. Ind. Electron.*, vol. 64, no. 3, pp. 1905–1915, Mar. 2017.

[21] J. K. Singh, K. A. Jaafari, R. K. Behera, K. A. Hosani, and U. R. Muduli, "Faster convergence controller with distorted grid conditions for photovoltaic grid following inverter system," *IEEE Access*, vol. 10, pp. 29834–29845, 2022.

[22] Y. Wang, H. Yu, and Y. Liu, "Speed-current single-loop control with overcurrent protection for PMSM based on time-varying nonlinear disturbance observer," *IEEE Trans. Ind. Electron.*, vol. 69, no. 1, pp. 179–189, Jan. 2022.

[23] L. Li, G. Pei, J. Liu, P. Du, L. Pei, and C. Zhong, "2-DOF robust H_∞ control for permanent magnet synchronous motor with disturbance observer," *IEEE Trans. Power Electron.*, vol. 36, no. 3, pp. 3462–3472, Mar. 2021.

[24] P. Kumar, A. R. Beig, D. V. Bhaskar, K. A. Jaafari, U. R. Muduli, and R. K. Behera, "An enhanced linear active disturbance rejection controller for high performance PMBLDCM drive considering iron loss," *IEEE Trans. Power Electron.*, vol. 36, no. 12, pp. 14087–14097, Dec. 2021.

[25] S. A. Khajehoddin, M. Karimi-Ghartemani, P. K. Jain, and A. Bakhshai, "DC-bus design and control for a single-phase grid-connected renewable converter with a small energy storage component," *IEEE Trans. Power Electron.*, vol. 28, no. 7, pp. 3245–3254, Jul. 2013.

[26] C. Zhang, X. Zhao, X. Wang, X. Chai, Z. Zhang, and X. Guo, "A grid synchronization PLL method based on mixed second- and third-order generalized integrator for DC offset elimination and frequency adaptability," *IEEE Trans. Emerg. Sel. Topics Power Electron.*, vol. 6, no. 3, pp. 1517–1526, Sep. 2018.

Jitendra Kumar Singh (Member, IEEE) received the B.E. degree in electrical and electronics engineering from the Bhopal Institute of Technology and Science, Bhopal, India, in 2010, and the M.E. degree in power electronics engineering from the Birla Institute of Technology Mesra, Ranchi, India, in 2016, and the Ph.D. degree in electrical engineering from the Indian Institute of Technology Patna, Patna, India, in 2023. He was a Visiting Scholar with the Department of Electrical Engineering and Computer Science, Khalifa University, Abu Dhabi, UAE, in 2022. He is currently with the Department of Wind and Energy Systems, Technical University of Denmark, Roskilde, Denmark. His research interests include control methods for power electronics converters in distribution systems, renewable energy interconnection, control issues in grid-connected systems and seamless power transfer.

Surya Prakash (Graduate Student Member, IEEE) received the B.Tech. degree in electrical and electronics engineering from the Jawaharlal Nehru Technological University, Hyderabad, India, in 2009, and the M.Tech. degree in power electronics engineering from the Visvesvaraya National Institute Of Technology, Nagpur, India, in 2012. He is currently working toward the Ph.D. degree in electrical engineering with the Indian Institute of Technology, Patna, Patna, India. He was a Visiting Scholar with the Department of Electrical Engineering and Computer Science, Khalifa University, Abu Dhabi, UAE, in 2023. His research interests include control methods for power electronics converters in distribution systems and renewable energy resources, grid interconnection issues, power quality enhancement, and low-voltage ride-through.

Khaled Al Jaafari (Senior Member, IEEE) received the B.Sc. and M.Sc. degrees in electrical engineering (EE) from Petroleum Institute, Abu Dhabi, UAE, in 2006 and 2011, respectively, and the Ph.D. degree from the Department of Electrical and Computer Engineering, Texas A&M University, College Station, TX, USA, in 2016. He is currently an Assistant Professor with the Khalifa University of Science and Technology, Abu Dhabi. His research interests include machines condition monitoring, power system analysis, power system protection, and power quality studies. He has two years (2006–2008) of experience in ZADCO as an Electrical Engineer with the upper Zakum Oil field platform, where he was part of the site facility and maintenance engineering team.

Ranjan Kumar Behera (Senior Member, IEEE) received the B.Eng. degree in electrical engineering from the Regional Engineering College Rourkela, Rourkela, India, in 1998, and the M.Tech. and Ph.D. degrees in electrical engineering from the Indian Institute of Technology Kanpur, Kanpur, India, in 2003 and 2009, respectively. Since 2009, he has been a Faculty Member and he is currently an Associate Professor with the Department of Electrical Engineering, Indian Institute of Technology Patna, Patna, India. His research interests include nonlinear control theory application to power electronic converters, pulse width modulation techniques, and multiphase electric drives control.

Dr. Behera was the recipient of the 2022 IEEE Outstanding Paper Award for the IEEE Transactions on Industrial Electronics.

Omar Al Zaabi (Member, IEEE) received the B.S., M.S., and Ph.D. degrees in electrical engineering from Pennsylvania State University, University Park, PA, USA, in 2012, 2014, and 2019, respectively. He is currently an Assistant Professor with the Department of Electrical and Computer Engineering, Khalifa University, Abu Dhabi, UAE. His research interests include electromagnetic characterization and measurement techniques, target tracking and radar cross-section (RCS) synthesis in addition to the use of applied electromagnetic in ecological and entomological applications.

Utkal Ranjan Muduli (Senior Member, IEEE) received the B.Tech. degree in electrical and electronics engineering from the Biju Patnaik University of Technology, Rourkela, India, in 2011, the M.Tech. degree in electrical engineering from the Indian Institute of Technology Gandhinagar, Palaj, India, in 2014, and the Ph.D. degree in electrical engineering from the Indian Institute of Technology Patna, Patna, India, in 2022.

He was a Visiting Scholar and a Research Associate with the Department of Electrical Engineering and Computer Science, Khalifa University, Abu Dhabi, UAE, in 2019 and 2021, respectively, where he is currently a Postdoctoral Research Fellow. His research interests include modulation strategies for multiphase motor drives, matrix converters and its control, battery power management, and wireless power transfer.

Dr. Muduli was the recipient of the 2022 IEEE Outstanding Paper Award for the IEEE Transactions on Industrial Electronics.

Khalifa Al Hosani (Senior Member, IEEE) received the B.Sc. and M.Sc. degrees in electrical engineering from the University of Notre Dame, Notre Dame, IN, USA, in 2005 and 2007, respectively, and the Ph.D. degree in electrical and computer engineering from Ohio State University, Columbus, OH, USA, in 2011. He is currently an Associate Professor with the Department of Electrical and Computer Engineering, Khalifa University, Abu Dhabi, UAE. He is the Co-founder of the Power Electronics and Advanced Sustainable Energy Center Laboratory, ADNOC Research and Innovation Center, Abu Dhabi. His research interests include a wide range of topics including nonlinear control, sliding mode control, control of power electronics, power systems stability and control, renewable energy systems modeling and control, smart grid, microgrid and distributed generation, and application of control theory to oil and gas applications.